



Contents lists available at ScienceDirect

Journal of Fluids and Structures

journal homepage: www.elsevier.com/locate/jfs

An experimental investigation of flow-induced vibration of high-side-ratio rectangular cylinders

Jisheng Zhao^{*}, Kerry Hourigan, Mark C. Thompson*Fluids Laboratory for Aeronautical and Industrial Research (FLAIR), Department of Mechanical and Aerospace Engineering, Monash University, Victoria 3800, Australia*

ARTICLE INFO

Article history:

Received 20 November 2018

Received in revised form 18 January 2019

Accepted 21 January 2019

Available online xxx

Keywords:

Fluid–structure interaction

Flow-induced vibration

Rectangular cylinders

ABSTRACT

This study reports an experimental investigation on the flow-induced vibration (FIV) of elastically mounted rectangular cylinders with *high-side-ratio* in free-stream flow. The side ratio (σ), defined as the ratio of the cross-flow side width (h) to the streamwise side width (b) of the cylinder, namely $\sigma = h/b$, was varied from 2.0 to 5.0. The fluid–structure system was modelled using a low-friction air-bearing system in conjunction with a free-surface water channel facility. The structural vibration was characterised over the reduced velocity range of $2 \leq U^* = U/(f_{nw}h) \leq 16$, where U is the free stream velocity and f_{nw} is the natural frequency of the system in quiescent water. The corresponding Reynolds number varied in the range of $940 \leq Re = Uh/\nu \leq 8200$, where ν is the fluid kinematic viscosity. The mass ratio, defined as the ratio of the oscillating mass to the displaced fluid mass, varied from 6.56 to 12.18, depending on the cylinder models. It was found that the vibration response was dominated by *vortex-induced vibration (VIV)* response for $U^* \lesssim 8.4$ for all the σ cases tested. In the VIV lock-in regime, the local peak amplitude response was found to increase with σ (i.e. from $A/h \simeq 1.05$ for $\sigma = 2.0$ to $A/h \simeq 1.69$ for $\sigma = 5.0$). Interestingly, beyond the VIV lock-in regime, while a galloping response was observed for the cases of $\sigma \leq 4.0$, where the vibration amplitude increased linearly with U^* , the $\sigma = 5.0$ case exhibited a bounded galloping regime with the amplitude increasing up to $A/h \simeq 1.44$ at $U^* = 10.8$, prior to an abrupt drop to $A/h \approx 0.35$ of a desynchronisation regime for higher U^* values. The results suggest that this unexpected collapse of galloping response could be due to exceeding the relative incidence angle threshold for possible galloping.

© 2019 Elsevier Ltd. All rights reserved.

1. Introduction

The dynamics of fluid–structure interaction is a subject which receives ongoing research attention due to its intrinsic nature in science and practical importance in engineering applications. In particular, flow-induced vibration (FIV) of structures is of great interest in the subject of fluid–structure interaction, due to its two-sided roles in engineering, one as a potential energy harvesting source (see Wang et al., 2017; Soti et al., 2018) and the other as a damaging phenomenon that can affect structural fatigue life and safety (e.g. the collapse of the original Tacoma Narrows Bridge in 1940). Fundamentally, two body oscillator phenomena typical of FIV are *vortex-induced vibration (VIV)* and *galloping* (Blevins, 1990; Naudascher and Rockwell, 2005). Structures that have rectangular cross-sections have been found to be susceptible to these two FIV phenomena.

^{*} Corresponding author.

E-mail address: jisheng.zhao@monash.edu (J. Zhao).

Fundamentally, VIV occurs as the periodic shedding of vortices formed from alternate sides of an elastic or elastically mounted body creates a fluctuating pressure distribution on the body to cause structural vibration. When the vortex shedding frequency is near the natural frequency of the system, it will deviate from that expected for a stationary body (i.e. the Strouhal vortex shedding frequency, denoted by f_{St}) and lock onto the body vibration frequency, resulting in vibration resonance with large-amplitude body oscillations. This behaviour is known as “lock-in” or synchronisation, which takes place over discrete flow velocity ranges. Since the pioneering experiments of Brooks (1960), circular cylinders have been adopted as the standard model in numerous studies of VIV (e.g. Feng, 1968; Khalak and Williamson, 1996, 1997a,b, 1999; Govardhan and Williamson, 2000; Carberry et al., 2001; Morse and Williamson, 2009; Zhao et al., 2014a, among others). It has been shown that VIV characteristics of a circular cylinder, including the vibration amplitude, frequency response and lock-in regime, are dependent on a number of factors of the structural properties and flow conditions, including the mass and damping ratios, flow reduced velocity, and Reynolds number (see Feng, 1968; Khalak and Williamson, 1996; Klamo et al., 2005; Govardhan and Williamson, 2006; Soti et al., 2018). Here, it should be noted that the mass ratio (m^*) is defined as the ratio of the total oscillating mass (m) to the displaced fluid mass (m_d), namely $m^* = m/m_d$; the reduced velocity is defined by $U^* = U/(f_n D)$, where U is the free-stream velocity, D is the cylinder diameter and f_n is the natural frequency of the system in quiescent fluid; the Reynolds number is defined by $Re = UD/\nu$, with ν the kinematic viscosity of the fluid. Comprehensive reviews on VIV of circular cylinders can be found in the articles of Sarpkaya (2004), Williamson and Govardhan (2004) and Gabbai and Benaroya (2005). Unlike VIV which is excited by the instability of vortex shedding, galloping, on the other hand, is often known as an aeroelastic instability that is induced by changes in the relative incidence angle by the movement of a structure of non-circular cross-section, resulting in an aerodynamic force instantaneously acting on the body in the same direction as the body movement. Typically, galloping oscillation is characterised by a nearly linear amplitude growth trend with increasing flow velocity at an oscillation frequency much lower than the vortex shedding frequency (see Bearman et al., 1987).

While the two FIV phenomena of rectangular cylinders have received considerable attention for systems with high mass ratios, much less research has been done at low mass-damping ratios. The majority of early studies have focused on galloping in wind flows, as motivated partly by applications in civil engineering, such as buildings and bridges. Based on the criterion of galloping instability given by Den Hartog (1932, 1956), Parkinson and Brooks (1961) and Parkinson and Smith (1964) developed a quasi-steady theory to successfully predict the galloping amplitude response at high reduced velocities for a square cylinder in both smooth and turbulent wind flows, where the influence of vortex shedding on galloping was negligible. However, other studies, including (Smith, 1962; Santosham, 1966), showed that the quasi-steady theory failed to predict the onset flow velocity for galloping of rectangular cylinders with other side ratios rather than unity (the square cylinder), due to the influence of vortex shedding and the *afterbody* (i.e. the structural part of a bluff body downstream of the flow separation points). It should be noted that the side ratio used in the present study is defined by $\sigma = h/b$, where b and h are the streamwise and cross-flow dimensions, respectively, of the rectangular cross-section as illustrated in Fig. 1. Evidently, the side ratio is an important parameter affecting the afterbody shape and size and thus affecting the vortex shedding frequency and wake structure (see Okajima, 1982, 1990; Norberg, 1993; Knisely, 1990; Mills et al., 2003). Moreover, as demonstrated by Novak (1972) and Novak and Tanaka (1974), flow turbulence also has significant effects on galloping instability. Intrinsically, combined VIV and galloping may occur under some conditions of the mass-damping parameter and reduced velocity (Parkinson and Wawzonek, 1981; Bearman et al., 1987; Corless and Parkinson, 1988, 1993). Furthermore, the interference of VIV and galloping has been investigated for low-side-ratio rectangular cylinders, again, in wind tunnel experiments (e.g. Mannini et al., 2014, 2016). However, the recent studies of Nemes et al. (2012), Zhao et al. (2014b) and Zhao et al. (2018c) demonstrated even more profound VIV-galloping interaction for low- m^* square cylinders with varying angle of attack in a water flow, suggesting that the afterbody and flow separation points were the key factors of the mechanisms. Interestingly, Bokaian and Geoola (1983, 1985) showed that VIV lock-in could suppress the galloping instability in the vicinity of $U^* = 1/St$ for a rectangular cylinder of $\sigma = 2$ with $m^* \simeq 16.8$ in water flow, where $St = f_{St} h/U$ is the Strouhal number for a fixed cylinder. More recently, Massai et al. (2018) showed that a low- m^* rectangular cylinder of $\sigma = 1.5$ exhibited a vibrational response similar to that of Bokaian and Geoola (1985), but different types of vibration response were encountered as the angle of attack was varied from 0° to 90° .

Clearly, the role of an afterbody could not be emphasised enough. However, our very recent study of D-section cylinders (Zhao et al., 2018a) has shown that an afterbody can affect the FIV response, but it is not essential for the occurrence of VIV at low mass and damping ratios. Interestingly, Zhao et al. (2019) showed that the peak vibration amplitude of elliptical cylinders increased substantially as the afterbody was reduced. Of interest to the current study, from a fundamental point of view, is the influence of an afterbody on the FIV response of rectangular cylinders with high side ratios ($2.0 \leq \sigma \leq 5.0$). This is examined by characterising the structural vibration amplitude and frequency, fluid forces and phases as a function of reduced velocity.

The following section Section 2 provides the experimental details. The results and discussion on the dynamic responses are presented in Section 3. Finally, conclusions are drawn in Section 4.

2. Experimental details

A schematic of the 1-DOF flow-structure system is given in Fig. 1. The body dynamics is governed by the linear second-order oscillator equation

$$m\ddot{y}(t) + c\dot{y}(t) + ky(t) = F_y(t), \quad (1)$$

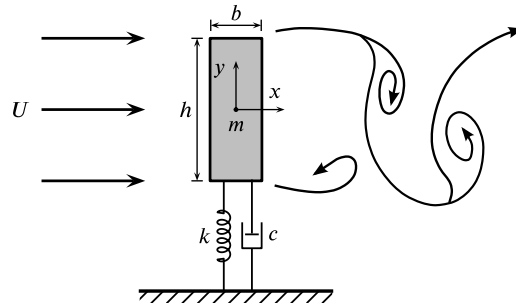


Fig. 1. Schematic of the fluid–structure system for the present study.

Table 1

The experimental parameters of the rectangular cylinders used in the present study.

σ	b [mm]	h [mm]	m [g]	m_d [g]	m^*	f_{na} [Hz]	f_{nw} [Hz]	ζ
2.0	12.50	25.00	1257.7	191.7	6.56	0.806	0.761	1.39×10^{-3}
2.5	10.00	25.00	1144.2	153.4	7.46	0.844	0.810	1.70×10^{-3}
3.1	8.00	25.00	1044.2	122.7	8.51	0.883	0.858	1.39×10^{-3}
4.0	6.25	25.00	987.2	95.9	10.29	0.909	0.887	1.34×10^{-3}
5.0	5.00	25.00	934.4	76.7	12.18	0.934	0.914	1.38×10^{-3}

where m is the total oscillating mass of the system, c the structural damping of the system, k the spring constant, $y(t)$ the body displacement, and $F_y(t)$ the transverse fluid force.

The flow–structure system was modelled based on a low-friction air bearing rig in conjunction with the free-surface recirculating water channel of the *Fluids Laboratory for Aeronautical and Industrial Research* (FLAIR) at Monash University. Details of this air bearing rig can be found in Zhao et al. (2018b). The test section of the water channel has dimensions of 600 mm in width, 800 mm in depth and 4000 mm in length. In the present experiments, the free-stream turbulence level was less than 1%. Details of the water channel facilities can be found in Nemes et al. (2012) and Zhao et al. (2014b).

In the present study, five rectangular cylinders with the side ratio ranging from 2.0 to 5.0 were tested (see Table 1 for parametric details). These rigid cylinder models were precision made from aluminium using CNC (computer numerical control) machining to manufacture the cross-sectional profiles with a tolerance of ± 0.010 mm. The cylinders were hard anodised against water corrosion. The immersed length of the cylinder was $L = 614$ mm, giving an aspect ratio of $L/h = 24.6$. It should be noted that the free end of the cylinders was positioned with a small clearance of ≈ 1 mm (or $4\%h$) above a platform placed on the water channel floor to reduce the end effects. This end-conditioning technique was first introduced by Khalak and Williamson (1996) for VIV of a circular cylinder. Details of the platform used in the present experiments can be found in Zhao et al. (2018a,b). The cylinders were mechanically fixed to an adaptor coupled with the air-bearing rig to prohibit their axial rotation, and the hydroelastic system was carefully positioned to ensure zero incidence angle. The total oscillating mass (m) and the displaced mass of the fluid ($m_d = \rho b h L$, with ρ the density of water) of all the σ cases are given in Table 1. Due to the loading limit of the present air-bearing rig, the mass ratio ($m^* = m/m_d$) was not able to be kept constant for all the cylinder models, and it varied from 6.56 for $\sigma = 2.0$ to 12.18 for $\sigma = 5.0$, while being of the order of $O(10)$. The natural frequencies of the system were measured by conducting free-decay tests individually in air and in quiescent water. The natural frequencies of the system in air (f_{na}) and in water (f_{nw}) are shown in Table 1, noting that the structural damping ratio is determined with consideration of the added mass (m_A) by $\zeta = c/2\sqrt{k(m + m_A)}$, where $m_A = ((f_{na}/f_{nw})^2 - 1)m$. In the present experiments, the structural damping ratios were found to be very low in the range of $1.34 \times 10^{-3} \leq \zeta \leq 1.70 \times 10^{-3}$, where it was expected that the FIV response was likely to be insensitive to ζ . More discussion on the effects of the mass and damping parameters on VIV of circular cylinders can be found in the studies of Govardhan and Williamson (2006) and Soti et al. (2018), while a generalised damping parameter for FIV is proposed in the article of Vandiver (2012).

The FIV response was investigated as a function of the reduced velocity ($U^* = U/(f_{nw}h)$). Table 2 shows the reduced velocity ranges, together with the corresponding Reynolds number ($Re = Uh/\nu$) ranges for the tested cylinders.

The body displacement was measured using a non-contact digital optical linear encoder (model: RGH24; Renishaw, UK) which had a resolution of $1 \mu\text{m}$ and a measurement range of ± 200 mm available. The transverse lift (F_y) acting on the vibrating cylinder was determined based on Eq. (1), with the body velocity (\dot{y}) and acceleration (\ddot{y}) derived from the body displacement (y). Validations of this method for the F_y measurement can be found in Zhao et al. (2014b, 2018b). For measurements at each U^* , signals were acquired at a sampling frequency of 100 Hz for 300 s (more than 100 vibration cycles). More details of the data acquisition system can be found in the related studies of Sareen et al. (2018) and Wong et al. (2017, 2018).

Table 2

The reduced velocity (U^*) and Reynolds number (Re) ranges investigated for the rectangular cylinders used in the present study.

σ	U^*	Re
2.0	2.2–16.0	980–7100
2.5	2.0–16.0	940–7520
3.1	2.0–16.0	990–7940
4.0	2.0–16.0	1025–8200
5.0	2.0–16.0	1050–7900

3. Results and discussion

3.1. Dynamic responses

Figs. 2 and 3 show the normalised vibration amplitude (A_{10}^*) together with the logarithmic-scale (normalised) power spectrum density (PSD) contours of the body oscillation frequency (f_y^*) and the transverse lift frequency ($f_{C_y}^*$), respectively. It should be noted that the normalised amplitude A_{10}^* represents the mean of the top 10% maximum amplitudes of A/h ; the coefficients of the transverse lift and vortex forces in this study are defined by $C_y = F_y / (\frac{1}{2} \rho U^2 h L)$ and $C_v = F_v / (\frac{1}{2} \rho U^2 h L)$, respectively, where the vortex force is decomposed based on $F_v = F_y - F_p$, with the potential force $F_p = -m_A \ddot{y}$ (see Lighthill, 1986; Govardhan and Williamson, 2000; Zhao et al., 2014a,b); the body oscillation frequency and the transverse lift frequency are normalised by the natural frequency in quiescent water, i.e., $f_y^* = f_y / f_{nw}$ and $f_{C_y}^* = f_{C_y} / f_{nw}$; the PSD presented is normalised by the local peak value at each U^* and then logarithmically scaled. More details of the construction method for the amplitude response and frequency PSD contours can be found in Zhao et al. (2014b).

As can be seen from Fig. 2(a), all the σ cases exhibit a VIV response characterised by an initial branch (IB) and a lock-in regime for low reduced velocities of $U^* \lesssim 8.4$, followed by a galloping response with the amplitude nearly increasing linearly with flow velocity. The boundaries of response regimes are determined by an overall examination of the amplitude response, frequency responses, fluid forces and phases. The term “initial branch” is adopted from the study of Khalak and Williamson (1996) who first characterised the VIV response of a circular cylinder with low $m^* - \zeta$ by three (“initial”, “upper” and “lower”) branches and a desynchronisation region. Similar to the VIV of a circular cylinder (see Khalak and Williamson, 1996; Zhao et al., 2014a), the body exhibits quasi-periodic oscillations in the initial branch, where the vibration frequency is influenced by the vortex shedding frequency and f_{nw} . To demonstrate this, Fig. 4(a) shows sample time traces at $U^* = 4.0$, $\sigma = 2.0$, where both the body vibration and the transverse lift appear to have unstable magnitudes, as their frequency is modulated by the vortex shedding frequency and f_{nw} (see (b) of Figs. 2 and 3). However, it is interesting to note that, when U^* is increased to a certain value, the body vibration frequency abruptly deviates from the trend of the Strouhal vortex shedding frequency and starts to lock onto a frequency close to f_{nw} , which is indicative of the onset of the lock-in regime. In the present experiment, the Strouhal number (for stationary cylinders) was observed to increase slightly with σ over the Re range tested, i.e. from $St = 0.142$ for $\sigma = 2.0$ to $St = 0.149$ for $\sigma = 5.0$, in good agreement with previous studies (e.g. Knisely, 1990). Nevertheless, it is found that the onset of lock-in tends to occur at a lower U^* as σ is increased, i.e., from $U^* \simeq 5.7$ for $\sigma = 2.0$ to $U^* \simeq 2.5$ for $\sigma = 5.0$. Clearly, the onset of lock-in occurs at a reduced velocity much lower than the theoretically expected value $U_r^* = 1/St$ for VIV resonance (i.e. f_{St} matches f_{nw}). This phenomenon is also seen in FIV of D-section cylinders with low mass-damping ratio (Zhao et al., 2018a).

In the VIV lock-in regimes, the body oscillations are highly periodic, with the dominant frequency of the body vibration matching that of the vortex shedding frequency. Sample time traces at $U^* = 6.0$, $\sigma = 2.0$ are presented in Fig. 4(b) demonstrating that the dynamics (i.e. the body vibration and fluid forcing) are highly periodic. It should also be noted that, as shown in Fig. 5, both the total phase (the phase angle between the transverse lift and the body displacement, denoted by ϕ_t) and the vortex phase (the phase angle between the vortex force and the body displacement, denoted by ϕ_v) appear to be close to either 0° or 180° in the lock-in regimes, meaning that fluid forcing is out of phase with the body velocity (\dot{y}) by approximately 90° , as opposed to galloping response that sees an aerodynamic force in phase with the body velocity. Moreover, the vibration amplitude appears to increase gradually with U^* to reach a local peak at $U^* \approx 1/St$ (see Fig. 2(a, b)), prior to a gradual and minor decline; the local A_{10}^* peak tends to increase as the afterbody is reduced with increases in σ ($A_{10}^* \simeq 1.05$ for $\sigma = 2.0$ and $A_{10}^* \simeq 1.69$ for $\sigma = 5.0$), despite increases in m^* . Table 3 shows a summary of the VIV lock-in ranges, together with the local A_{10}^* peak values, for the σ cases tested. Furthermore, the present cases exhibit much higher oscillation amplitudes and wider lock-in regions than the case of a square cylinder ($\sigma = 1$) studied by Zhao et al. (2014b), where a very narrow VIV resonance region was observed at $U^* \approx 6$. The present results thereby suggest that the afterbody plays an important role affecting the VIV response of a rectangular cylinder.

As U^* is further increased, the body vibration appears to be dominated by galloping for the cases of $2.00 \leq \sigma \leq 4.00$ at the remaining reduced velocities ($8.4 < U^* \leq 16$), which is characterised by a linear growth in the A_{10}^* response. While the dominant component of f_y^* increases slightly from the VIV lock-in frequency to a constant value slightly higher than f_{nw} (due to the added mass effect), the $f_{C_y}^*$ responses exhibit multiple frequency components, with one broad spectrum band following a trend slightly higher than that of f_{St} and the others matching closely to $2f_{nw}$ and $3f_{nw}$. As demonstrated by sample

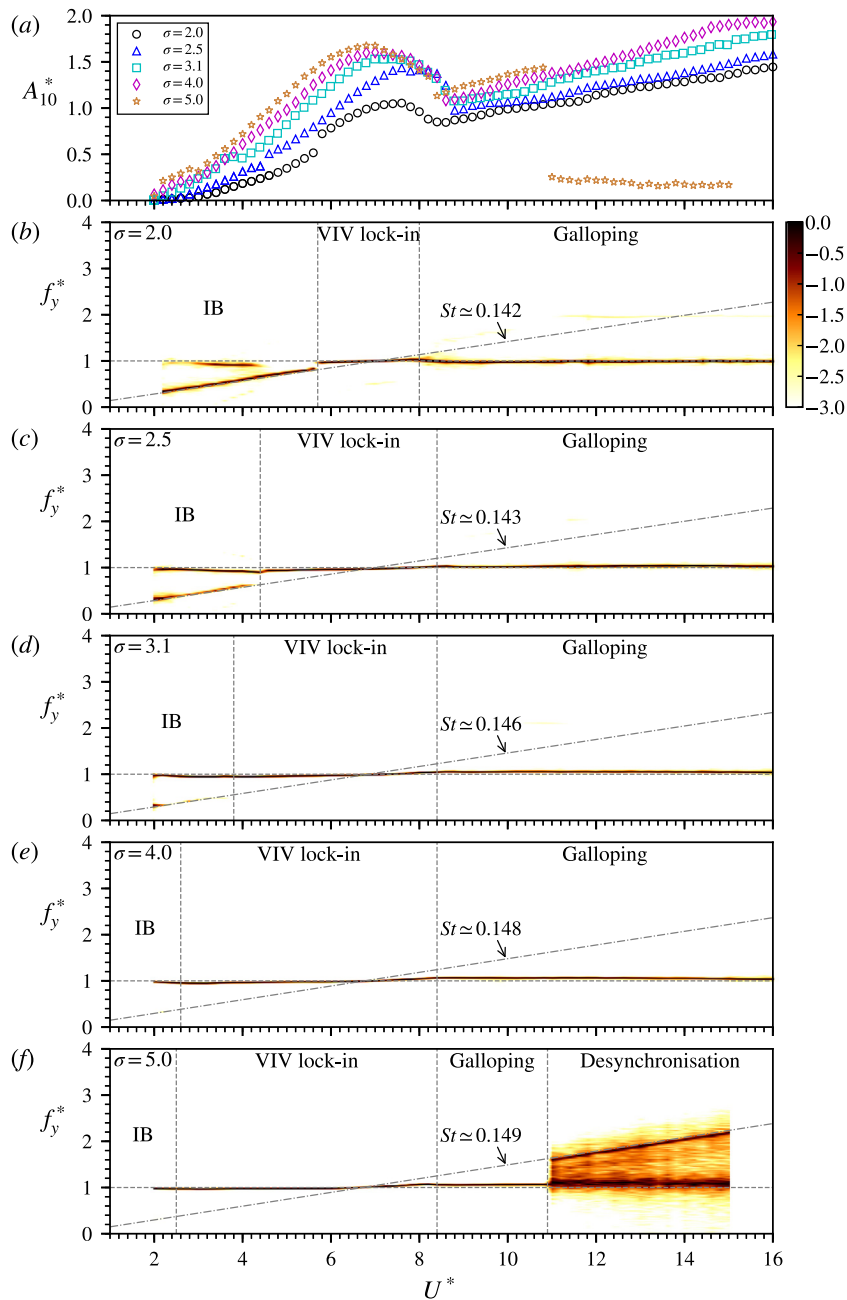


Fig. 2. The normalised amplitude response and logarithmic-scale PSD contours of the normalised vibration frequency (f_y^*) as a function of U^* for different σ values. In (b)–(f), the horizontal dashed line highlights the natural frequency, the vertical dashed lines represent the boundaries of different response regimes (i.e. the initial branch (IB), VIV lock-in, galloping, and desynchronisation), while the dot-dashed line represents the St value measured for a stationary cylinder.

time traces at $U^* = 9.0$ and 16.0 in Fig. 4(c, d), the body oscillations appear to be fairly periodic, whereas the fluid forces are of much lower periodicity as influenced by much higher frequency components, resulting in “slipping” behaviour in both ϕ_t and ϕ_v through 360° as time varies when the vibration amplitude becomes substantially larger at high velocity (i.e. $U^* = 16$). This indicates that the body oscillation frequency is not synchronised with the vortex shedding frequency, and as a result the large-scale body oscillations are dominated by galloping rather than VIV. In general, the amplitude responses of the cases of $\sigma \leq 4.0$ are similar to that of the $\sigma = 1.50$ case ($m^* = 2.24$) reported by Massai et al. (2018). Moreover, the present $\sigma = 2.0$ case agrees well with the previous experiments with the same side ratio ($\sigma = 2.0$, $L/h = 22.4$) and a higher mass ratio of $m^* \approx 16.8$ ($\zeta = 4.32 \times 10^{-2}$) conducted in the Reynolds number range of $700 < Re < 5000$ by Bokaian and

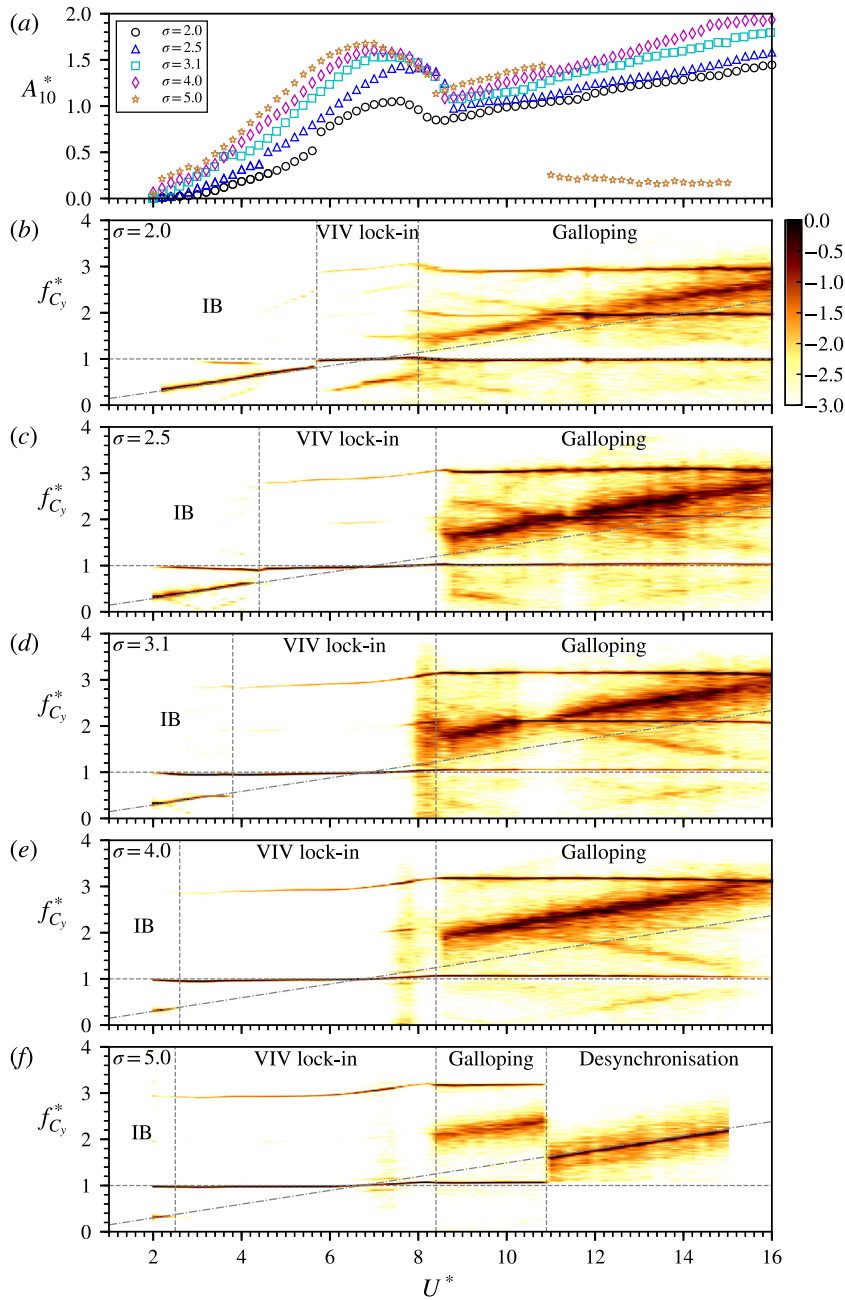


Fig. 3. The logarithmic-scale PSD contours of the normalised transverse lift frequency ($f_{C_y}^*$) as a function of U^* for different σ values. (a) revisits the A_{10}^* responses. For more details, see the caption of Fig. 2.

Table 3
The VIV lock-in ranges and the local A_{10}^* peak values observed for the rectangular cylinders tested.

σ	U^* (VIV lock-in)	Re (VIV lock-in)	A_{10}^* (VIV peak)	U^* (VIV peak)	Re (VIV peak)
2.0	5.7–8.0	2530–3550	1.05	7.6	3370
2.5	4.4–8.4	2070–3950	1.44	7.6	3570
3.1	3.8–8.4	1885–4170	1.53	7.4	3675
4.0	2.6–8.4	1330–4300	1.60	7.0	3585
5.0	2.4–8.4	1260–4420	1.69	6.8	3580

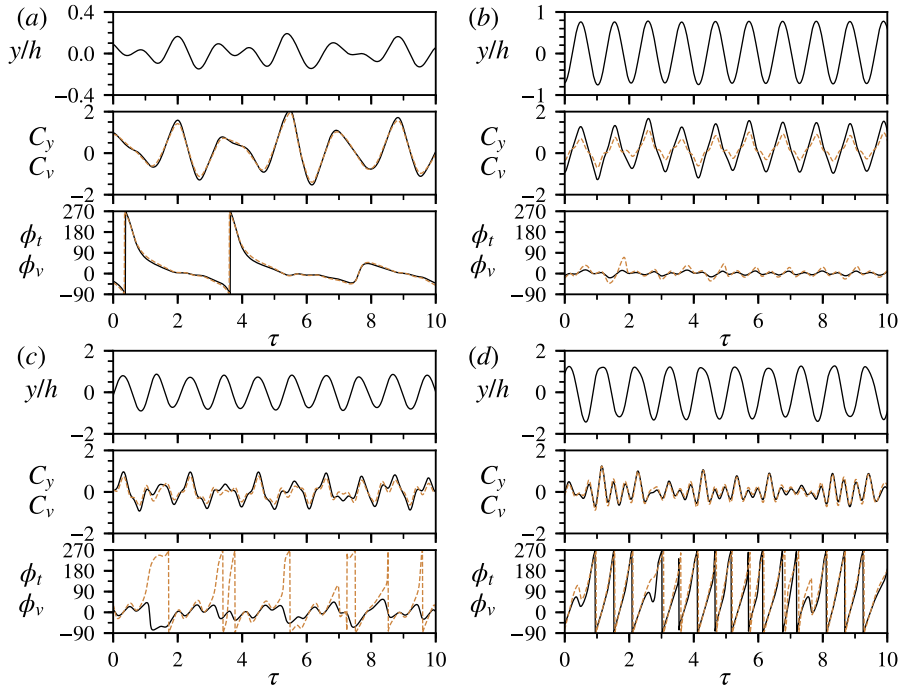


Fig. 4. Sample time traces of the body displacement (y/h), fluid force coefficients (C_y and C_v) and phases (ϕ_t and ϕ_v) at different reduced velocities for $\sigma = 2.0$: (a) $U^* = 4.0$, (b) $U^* = 6.0$, (c) $U^* = 9.0$ and (d) $U^* = 16.0$, showing that the dynamics change with the increase in U^* . Note that the phases ϕ_t and ϕ_v are presented in degrees. $\tau = f_{nw}t$ is the normalised time.

Geola (1985), in terms of the overall amplitude response and magnitude of the amplitude peak in the VIV lock-in regime, as well as the onset U^* of galloping. This implies that, in the tested Reynolds number ranges, the FIV response of the present σ cases is likely to be insensitive to the mass ratio effect, at least within the tested m^* range ($6 < m^* < 12$). Similar to the VIV region, the galloping oscillation amplitude in general also tends to increase with increasing σ .

Of particular interest here is the galloping response for $\sigma = 5.0$ that exhibits a linear amplitude growth up to $A_{10}^* \simeq 1.44$ at $U^* = 10.8$, prior to a sudden drop to a VIV desynchronisation region with $A_{10}^* \approx 0.35$ at higher U^* values. This sudden collapse of galloping is unexpected, as the fluid–structure interaction of this σ case appears to be much stronger (e.g. with a much wider lock-in regime and larger oscillations) than that of the $\sigma = 2.0$ case before the collapse ($U^* \leq 10.8$), while Bokaian and Geola showed that galloping persisted with an unrestricted oscillation amplitude growth for U^* up to 14π . As demonstrated by Zhao et al. (2018a), assuming that the body is oscillating at f_{nw} , the body vibration can be approximated as a sinusoidal motion, $y/h = (A/h) \sin(2\pi f_{nw}t)$; differentiating this motion equation gives the relative incidence angle $\alpha' = \dot{y}/U = 2\pi(A/h)hf_{nw} \cos(2\pi f_{nw}t)/U \Rightarrow \alpha'_{max} = \tan^{-1}(2\pi A^*/U^*)$. Taking the amplitude values of $A_{10}^* = 1.44$ at $U^* = 10.8$ for $\sigma = 5.0$, prior to the galloping collapse, gives $\alpha'_{max} \simeq 40^\circ$. Similarly, for $\sigma = 2.0$, α'_{max} is found to be approximately 37° at $U^* = 16.0$, while it is estimated to be 26° for $A^* \approx 3.5$ at $U^* \approx 14\pi$ reported by Bokaian and Geola. These results suggest that the U^* range where galloping occurs may be restricted by a relative incidence angle threshold which is dependent on the galloping instability of the geometric shape and afterbody and flow conditions (e.g. the Reynolds number and turbulence level). Given a relative incidence angle threshold, the collapse of galloping would be expected to occur at a higher reduced velocity for a lower f_{nw} under the same geometric and flow conditions.

Fig. 5 shows the root-mean-square (rms) coefficients of the transverse lift and vortex forces and also the corresponding phases. As σ increases, both C_y^{rms} and C_v^{rms} in the VIV-dominated regions tend to decrease, and their peak values tend to occur at a lower U^* when both ϕ_t and ϕ_v become consistent at 0° . After reaching their peaks, both C_y^{rms} and C_v^{rms} decrease rapidly to their local minima as U^* is increased to the end of the VIV-dominated region in each σ case. As galloping oscillations gradually become dominant at higher reduced velocities, both C_y^{rms} and C_v^{rms} increase slightly and then remain relatively stable. On the other hand, both ϕ_t and ϕ_v in the cases of $2.00 \leq \sigma \leq 4.00$ tend to approach 90° as U^* increases, which means that the driving force (F_y) gradually becomes in phase with the body speed (\dot{y}) favouring galloping oscillations. It should be noted that the body vibrations in the galloping-dominated region of all the σ cases is still influenced considerably by the vortex shedding. This is demonstrated in the next section Section 3.2.

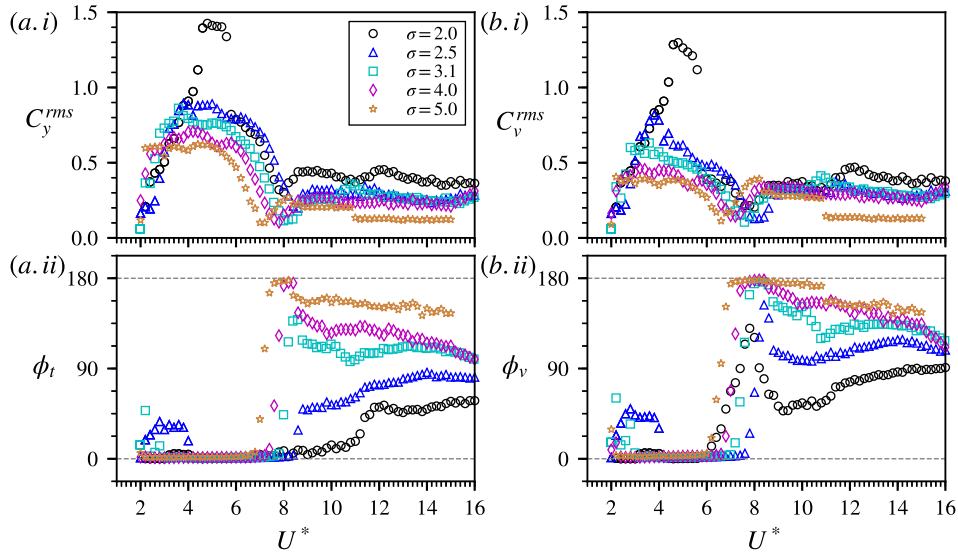


Fig. 5. The coefficients and phases of the transverse lift and vortex forces as a function of U^* for all the σ cases tested. Note the phases are presented in degrees.

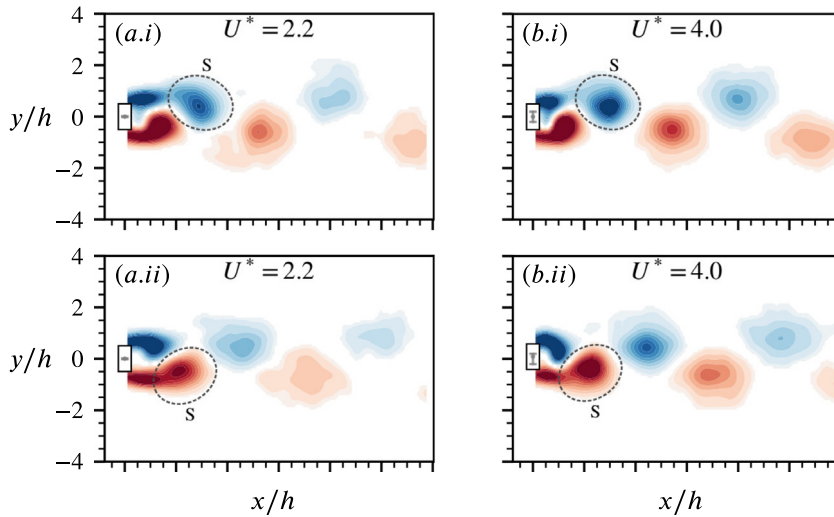


Fig. 6. Phase-averaged vorticity contours showing 2S patterns at (a) $U^* = 2.2$ and (b) $U^* = 4.0$ in the initial branch. As shown in these two cases, a single (S) vortex is shed per half cycle. The normalised vorticity range shown here is given by $\omega_z^* = \omega_z b/U \in [-4, 4]$, where ω_z is the vorticity out of the x - y plane. In each plot, the vertical line between two horizontal bars in grey represents the peak-to-peak vibration amplitude; the dot in grey represents the body centre position.

3.2. Wake structures for $\sigma = 2.0$

To gain a better understanding of the fluid–structure interaction, the wake structure of $\sigma = 2.0$ as a representative case is examined using spot PIV (particle image velocimetry) measurements at the following reduced velocities, $U^* \in \{2.0, 4.0, 5.0, 6.0, 7.0, 9.0, 12.0, 16.0\}$. Details of the PIV system used in the present study can be found in Zhao et al. (2018b).

Fig. 6 shows the phase averaged vorticity contours at $U^* = 2.2$ and 4.0. These two U^* values are selected from the initial branch of VIV, where low oscillation amplitudes are observed and the body vibration frequency is strongly influenced by the interaction between the Strouhal vortex shedding frequency and the natural frequency of the system. Clearly, a 2S wake mode consisting of two opposite-signed single (S) vortices shed per oscillation cycle (see Williamson and Roshko, 1988) is encountered, which is similar to the case a circular cylinder in the VIV initial branch (see Govardhan and Williamson, 2000; Zhao et al., 2014a).

As U^* is further increased to 5.0 (Fig. 7(a)), which is still located in the initial branch region, the flow structure around the body exhibits noticeable changes: as the body reaches its top position, two clockwise (CW) vortices are formed but then

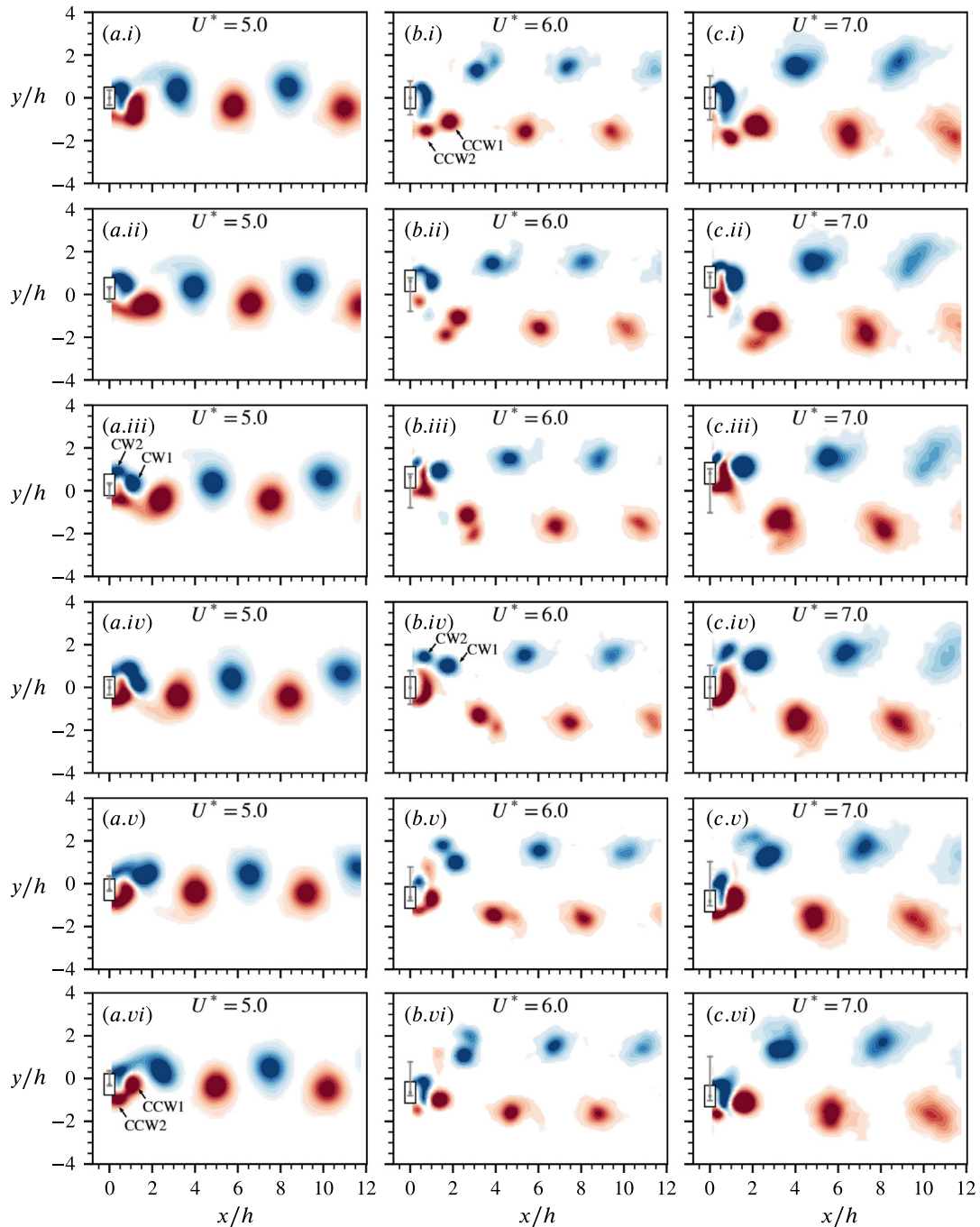


Fig. 7. Evolution of phase-averaged vorticity contours at (a) $U^* = 5.0$ (initial branch), (b) $U^* = 6.0$ (VIV lock-in) and (c) $U^* = 7.0$ (VIV lock-in). For more details, see the caption of Fig. 6.

merge quickly in the downstream as the body moves downwards to its equilibrium position; symmetrically, two counter-clockwise (CCW) vortices are formed at the body's bottom position. Nevertheless, the far wake appears to be a 2S pattern as seen previously in Fig. 6. However, at $U^* = 6.0$ and 7.0 as shown in Fig. 7(b, c), where large oscillations occur due to lock-in, the CCW and CW vortices in pairs are shed at the body's equilibrium position (e.g. Fig. 7(b.i) and (b.iv)); however, the same-signed vortices in pairs merge at $x/b \approx 3$, forming a two-row 2S pattern in the far wake.

As shown in Fig. 8, for higher reduced velocities $U^* = 9.0, 12.0$ and 16.0 in the galloping region, vortices are shed from shear layers elongated by large vibration amplitudes; however, the vortices are not well defined as they break up quickly in

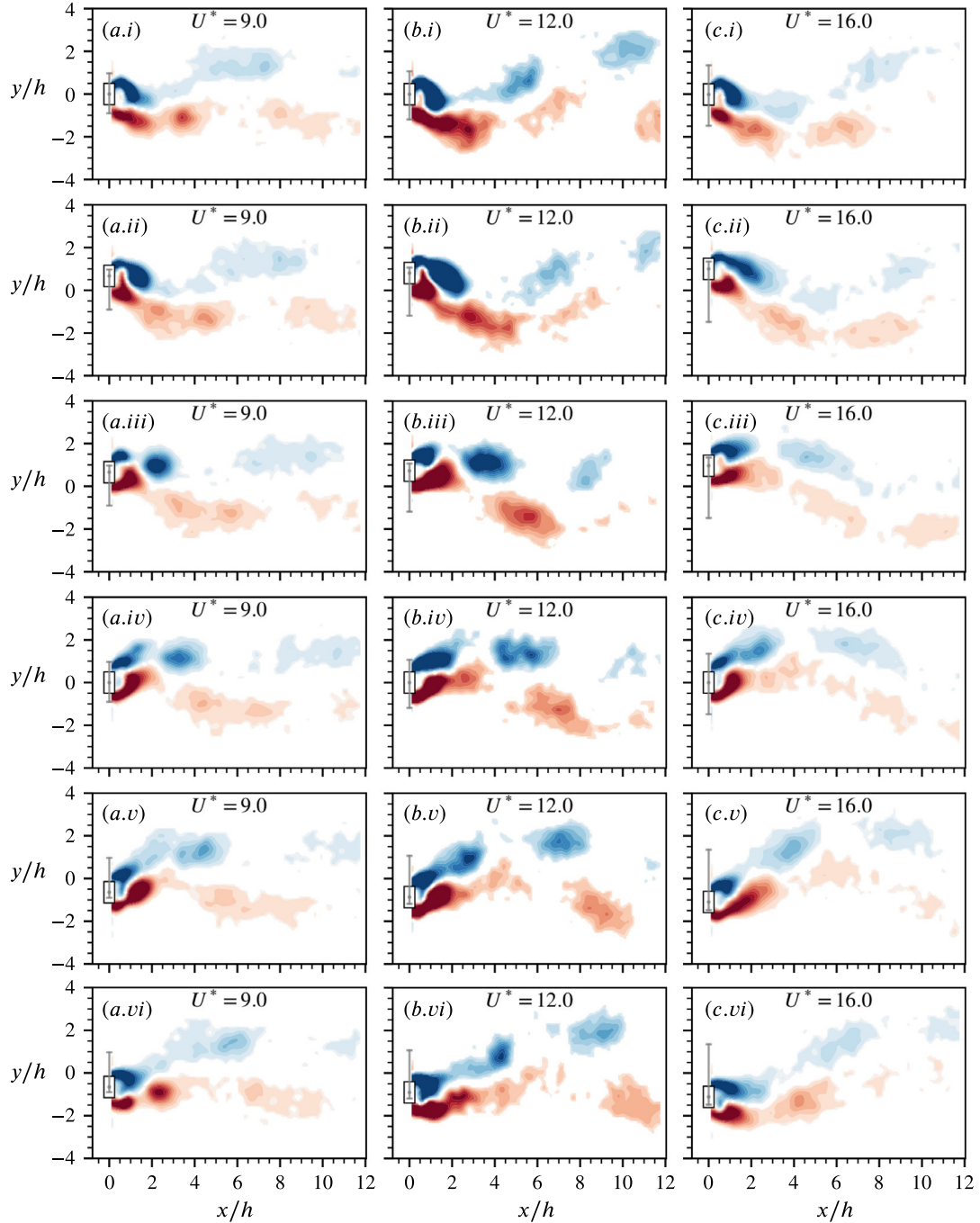


Fig. 8. Evolution of phase-averaged vorticity contours in the galloping-dominated region at $U^* = 9.0, 12.0$ and 16.0 in (a), (b) and (c) respectively. For more details, see the caption of Fig. 6.

the wake. Such a vortex shedding mode could contribute to the harmonic components and also broadband noise in the $f_{C_y}^*$ responses.

4. Conclusions

The transverse flow-induced vibration of rectangular cylinders has been experimentally investigated for the side ratios of $2.0 \leq \sigma \leq 5.0$ over a reduced velocity range of $2 \leq U^* \leq 16$.

It was found that the vibration response was dominated by VIV response which was characterised by an initial branch and a lock-in regime at low velocities of $U^* \lesssim 8.4$ for all the σ cases tested. As σ was increased, the onset of lock-in tended to occur at a lower reduced velocity, i.e., from $U^* \simeq 5.7$ for $\sigma = 2.0$ to $U^* \simeq 2.5$ for $\sigma = 5.0$. This is different from the VIV of a circular cylinder that sees the lock-in onset at $U^* \simeq 1/St$. Moreover, the local A_{10}^* peak value tended to increase with σ , i.e., $A_{10}^* \simeq 1.05$ for $\sigma = 2.0$ and $A_{10}^* \simeq 1.69$ for $\sigma = 5.0$. While the cases of $2.0 \leq \sigma \leq 4.0$ exhibited a galloping response with a linear amplitude growth with U^* up to the highest U^* tested, the $\sigma = 5.0$ case displayed galloping oscillation over a narrow reduced velocity range of $8.4 \leq U^* \leq 10.8$, prior to a sudden change to a desynchronisation region at higher U^* values. This suggests that the U^* range of galloping occurrence could be restricted by relative incidence angle. Similar to the VIV response regimes, the body vibration amplitude in galloping also tended to increase with σ . On the other hand, the galloping oscillation frequency, while remaining close to f_{nw} , was found to increase slightly with σ . Furthermore, from the PIV measurements for $\sigma = 2.0$, it is found that the initial branch and lock-in regime exhibit pure VIV features with well-defined vortices periodically shed into the wake. In the galloping region, however, vortices shed from elongated shear layers break up quickly in the wake, contributing to harmonic frequencies with the dominant component much higher than those of the body vibration.

It would be of further interest to assess the galloping instability of the rectangular cylinders through quasi-steady approach and extended experiments with wake measurements, which would be useful to explain the galloping collapse for $\sigma = 5.0$. This galloping collapse provides a good starting point for future research to explore the FIV response for higher side ratios ($\sigma > 5$). Future studies should also investigate the influence of the mass ratio, damping ratio, and Reynolds number on the FIV response of rectangular cylinders, e.g., via new experimental designs or numerical simulations that allow these parameters to be kept constant.

Acknowledgement

The support from Australian Research Council Discovery Project grants DP150102879 and DP170100275 is gratefully acknowledged.

References

- Bearman, P.W., Gartshore, I.S., Maull, D., Parkinson, G.V., 1987. Experiments on flow-induced vibration of a square-section cylinder. *J. Fluids Struct.* 1 (1), 19–34.
- Blevins, R.D., 1990. *Flow-Induced Vibration*, second ed. Krieger Publishing Company, Malabar.
- Bokaian, A., Geoola, F., 1983. On the cross flow response of cylindrical structures. *Proc. Inst. Civ. Eng.* 75 (3), 397–418.
- Bokaian, A., Geoola, F., 1985. Effects of vortex-resonance on nearby galloping instability. *J. Eng. Mech.* 111 (5), 591–609.
- Brooks, P.H.N., 1960. Experimental Investigation of the Aeroelastic Instability of Bluff Two-Dimensional Cylinders (M.A.Sc.), University of British Columbia.
- Carberry, J., Sheridan, J., Rockwell, D., 2001. Force and wake modes of an oscillating cylinder. *J. Fluids Struct.* 15, 523–532.
- Corless, R., Parkinson, G.V., 1988. A model of the combined effects of vortex-induced oscillation and galloping. *J. Fluids Struct.* 2 (3), 203–220.
- Corless, R.M., Parkinson, G.V., 1993. Mathematical modelling of the combined effects of vortex-induced vibration and galloping. Part II. *J. Fluids Struct.* 7, 825–848.
- Den Hartog, J.P., 1932. Transmission line vibration due to sleet. *Trans. Am. Inst. Electr. Eng.* 51 (4), 1074–1076.
- Den Hartog, J.P., 1956. *Mechanical Vibrations*. McGraw-Hill.
- Feng, C.C., 1968. The Measurement of Vortex Induced Effects in Flow Past Stationary and Oscillating Circular and D-Section Cylinders (Master's thesis), The University of British Columbia.
- Gabbai, R., Benaroya, H., 2005. An overview of modeling and experiments of vortex-induced vibration of circular cylinders. *J. Sound Vib.* 282 (3–5), 575–616.
- Govardhan, R., Williamson, C.H.K., 2000. Modes of vortex formation and frequency response of a freely vibrating cylinder. *J. Fluid Mech.* 420, 85–130.
- Govardhan, R., Williamson, C.H.K., 2006. Defining the 'modified Griffin plot' in vortex-induced vibration: revealing the effect of Reynolds number using controlled damping. *J. Fluid Mech.* 561, 147–180.
- Khalak, A., Williamson, C.H.K., 1996. Dynamics of a hydroelastic cylinder with very low mass and damping. *J. Fluids Struct.* 10 (5), 455–472.
- Khalak, A., Williamson, C.H.K., 1997a. Fluid forces and dynamics of a hydroelastic structure with very low mass and damping. *J. Fluids Struct.* 11 (8), 973–982.
- Khalak, A., Williamson, C.H.K., 1997b. Investigation of relative effects of mass and damping in vortex-induced vibration of a circular cylinder. *J. Wind Eng. Ind. Aerodyn.* 69, 341–350.
- Khalak, A., Williamson, C.H.K., 1999. Motions, forces and mode transitions in vortex-induced vibrations at low mass-damping. *J. Fluids Struct.* 13 (7–8), 813–851.
- Klamo, J.T., Leonard, A., Roshko, A., 2005. On the maximum amplitude for a freely vibrating cylinder in cross-flow. *J. Fluids Struct.* 21 (4), 429–434.
- Knisely, C.W., 1990. Strouhal numbers of rectangular cylinders at incidence: a review and new data. *J. Fluids Struct.* 4 (4), 371–393.
- Lighthill, J., 1986. Fundamentals concerning wave loading on offshore structures. *J. Fluid Mech.* 173, 667–681.
- Mannini, C., Marra, A.M., Bartoli, G., 2014. VIV-galloping instability of rectangular cylinders: review and new experiments. *J. Wind Eng. Ind. Aerodyn.* 132, 109–124.
- Mannini, C., Marra, A.M., Massai, T., Bartoli, G., 2016. Interference of vortex-induced vibration and transverse galloping for a rectangular cylinder. *J. Fluids Struct.* 66, 403–423.
- Massai, T., Zhao, J., Jacono, D.L., Bartoli, G., Sheridan, J., 2018. The effect of angle of attack on flow-induced vibration of low-side-ratio rectangular cylinders. *J. Fluids Struct.* 82, 375–393.
- Mills, R., Sheridan, J., Hourigan, K., 2003. Particle image velocimetry and visualization of natural and forced flow around rectangular cylinders. *J. Fluid Mech.* 478, 299–323.
- Morse, T.L., Williamson, C.H.K., 2009. Prediction of vortex-induced vibration response by employing controlled motion. *J. Fluid Mech.* 634, 5–39.
- Naudascher, E., Rockwell, D., 2005. *Flow-Induced Vibrations: An Engineering Guide*. Dover Publications.
- Nemes, A., Zhao, J., Lo Jacono, D., Sheridan, J., 2012. The interaction between flow-induced vibration mechanisms of a square cylinder with varying angles of attack. *J. Fluid Mech.* 710, 102–130.
- Norberg, C., 1993. Flow around rectangular cylinders: pressure forces and wake frequencies. *J. Wind Eng. Ind. Aerodyn.* 49 (1–3), 187–196.
- Novak, M., 1972. Galloping oscillations of prismatic structures. *J. Eng. Mech. Div.* 98, 27–46.

- Novak, M., Tanaka, H., 1974. Effect of turbulence on galloping instability. *J. Eng. Mech. Div.* 100 (1), 27–47.
- Okajima, A., 1982. Strouhal numbers of rectangular cylinders. *J. Fluid Mech.* 123, 379–398.
- Okajima, A., 1990. Numerical simulation of flow around rectangular cylinders. *J. Wind Eng. Ind. Aerodyn.* 33 (1–2), 171–180.
- Parkinson, G.V., Brooks, N.P.H., 1961. On the aeroelastic instability of bluff cylinders. *J. Appl. Mech.* 28 (2), 252–258.
- Parkinson, G.V., Smith, J.D., 1964. The square prism as an aeroelastic non-linear oscillator. *Quart. J. Mech. Appl. Math.* 17 (2), 225–239.
- Parkinson, G.V., Wawzonek, M.A., 1981. Some considerations of combined effects of galloping and vortex resonance. *J. Wind Eng. Ind. Aerodyn.* 8 (1–2), 135–143.
- Santosham, T.V., 1966. Force Measurements on Bluff Cylinders and Aeroelastic Galloping of a Rectangular Cylinder (Master's thesis), University of British Columbia.
- Sareen, A., Zhao, J., Jacono, D.L., Sheridan, J., Hourigan, K., Thompson, M.C., 2018. Vortex-induced vibration of a rotating sphere. *J. Fluid Mech.* 837, 258–292.
- Sarpkaya, T., 2004. A critical review of the intrinsic nature of vortex-induced vibrations. *J. Fluids Struct.* 19 (4), 389–447.
- Smith, J.D., 1962. An Experimental Study of the Aeroelastic Instability of Rectangular Cylinders (Ph.D. thesis), University of British Columbia.
- Soti, A.K., Zhao, J., Thompson, M.C., Sheridan, J., Bhardwaj, R., 2018. Damping effects on vortex-induced vibration of a circular cylinder and implications for power extraction. *J. Fluids Struct.* 81, 289–308.
- Vandiver, J.K., 2012. Damping parameters for flow-induced vibration. *J. Fluids Struct.* 35, 105–119.
- Wang, Z., Du, L., Zhao, J., Sun, X., 2017. Structural response and energy extraction of a fully passive flapping foil. *J. Fluids Struct.* 72, 96–113.
- Williamson, C.H.K., Govardhan, R., 2004. Vortex-induced vibration. *Annu. Rev. Fluid Mech.* 36, 413–455.
- Williamson, C.H.K., Roshko, A., 1988. Vortex formation in the wake of an oscillating cylinder. *J. Fluids Struct.* 2 (4), 355–381.
- Wong, K.W.L., Zhao, J., Lo Jacono, D., Thompson, M.C., Sheridan, J., 2017. Experimental investigation of flow-induced vibration of a rotating circular cylinder. *J. Fluid Mech.* 829, 486–511.
- Wong, K.W.L., Zhao, J., Lo Jacono, D., Thompson, M.C., Sheridan, J., 2018. Experimental investigation of flow-induced vibration of a sinusoidally rotating circular cylinder. *J. Fluid Mech.* 848, 430–466.
- Zhao, J., Hourigan, K., Thompson, M.C., 2018a. Flow-induced vibration of D-section cylinders: an afterbody is not essential for vortex-induced vibration. *J. Fluid Mech.* 851, 317–343.
- Zhao, J., Hourigan, K., Thompson, M.C., 2019. Dynamic response of elliptical cylinders undergoing transverse flow-induced vibration. *J. Fluids Struct.* <http://dx.doi.org/10.1016/j.jfluidstructs.2019.01.011>, (in press).
- Zhao, J., Leontini, J.S., Lo Jacono, D., Sheridan, J., 2014a. Chaotic vortex induced vibrations. *Phys. Fluids* 26 (12), 121702.
- Zhao, J., Leontini, J.S., Lo Jacono, D., Sheridan, J., 2014b. Fluid–structure interaction of a square cylinder at different angles of attack. *J. Fluid Mech.* 747, 688–721.
- Zhao, J., Lo Jacono, D., Sheridan, J., Hourigan, K., Thompson, M.C., 2018b. Experimental investigation of in-line flow-induced vibration of a rotating cylinder. *J. Fluid Mech.* 847, 664–699.
- Zhao, J., Nemes, A., Lo Jacono, D., Sheridan, J., 2018c. Branch/mode competition in the flow-induced vibration of a square cylinder. *Philos. Trans. R. Soc. Lond. Ser. A* 376, 20170243.